eprints@whiterose.ac.uk
https://eprints.whiterose.ac.uk/

Background modeling for dark matter search with 1.7 years of COSINE-100 data

G. Adhikari[1,15]**, P. Adhikari**[1]**, E. Barbosa de Souza**[2]**, N. Carlin**[3]**,**
J.J. Choi[4]**, S. Choi**[4]**, M. Djamal**[5]**, A.C. Ezeribe**[6]**, L.E. França**[3]**, C. Ha**[7]**,**
I.S. Hahn[8]**, E.J. Jeon**[a,7]**, J.H. Jo**[2]**, W.G. Kang**[7]**, M. Kauer**[9]**, G.S. Kim**[10]**,**
H. Kim[7]**, H.J. Kim**[10]**, K.W. Kim**[7]**, N.Y. Kim**[7]**, S.K. Kim**[4]**, Y.D. Kim**[7,1,11]**,**
Y.H. Kim[7,12,11]**, Y.J. Ko**[b,7]**, V.A. Kudryavtsev**[6]**, E.K. Lee**[7]**, H.S. Lee**[7,11]**,**
J. Lee[7]**, J.Y. Lee**[4]**, M.H. Lee**[7,11]**, S.H. Lee**[11]**, D.S. Leonard**[7]**, W.A. Lynch**[6]**,**
B.B. Manzato[3]**, R.H. Maruyama**[2]**, R.J. Neal**[6]**, S.L. Olsen**[7]**, H.K. Park**[13]**,**
H.S. Park[12]**, K.S. Park**[7]**, R.L.C. Pitta**[3]**, H. Prihtiadi**[5]**, S.J. Ra**[7]**, C. Rott**[14]**,**
K.A. Shin[7]**, A. Scarff**[6]**, N.J.C. Spooner**[6]**, W.G. Thompson**[2]**, L. Yang**[15]**,**
G.H. Yu[14]

[1]Department of Physics and Astronomy, Sejong University, Seoul 05006, Republic of Korea
[2]Wright Laboratory, Department of Physics, Yale University, New Haven, CT 06520, USA
[3]Physics Institute, University of São Paulo, 05508-090, São Paulo, Brazil
[4]Department of Physics and Astronomy, Seoul National University, Seoul 08826, Republic of Korea
[5]Department of Physics, Bandung Institute of Technology, Bandung 40132, Indonesia
[6]Department of Physics and Astronomy, University of Sheffield, Sheffield S3 7RH, United Kingdom
[7]Center for Underground Physics, Institute for Basic Science (IBS), Daejeon 34126, Republic of Korea
[8]Department of Science Education, Ewha Womans University, Seoul 03760, Republic of Korea
[9]Department of Physics and Wisconsin IceCube Particle Astrophysics Center, University of Wisconsin-Madison, Madison, WI 53706, USA
[10]Department of Physics, Kyungpook National University, Daegu 41566, Republic of Korea
[11]IBS School, University of Science and Technology (UST), Daejeon 34113, Republic of Korea
[12]Korea Research Institute of Standards and Science, Daejeon 34113, Republic of Korea
[13]Department of Accelerator Science, Graduate School, Korea University, Sejong 30019, Republic of Korea
[14]Department of Physics, Sungkyunkwan University, Seoul 16419, Republic of Korea
[15]Department of Physics, University of California, San Diego, La Jolla, CA 92093, USA

Abstract We present a background model for dark matter searches using an array of NaI(Tl) crystals in the COSINE-100 experiment that is located in the Yangyang underground laboratory. The model includes background contributions from both internal and external sources, including cosmogenic radionuclides and surface ^{210}Pb contamination. To improve the model in the low energy region, with the threshold lowered to 1 keV, we used a depth profile of ^{210}Pb contamination in the surface of the NaI(Tl) crystals determined in a comparison between measured and simulated spectra. We also considered the effect of the energy scale errors propagated from the statistical uncertainties and the nonlinear detector response at low energies. The 1.7 years COSINE-100 data taken between October 21, 2016 and July 18, 2018 were used for this analysis. The Geant4 toolkit version 10.4.2 was utilized throughout the Monte Carlo simulations for the possible internal and external origins. In particular, the version provides a non-Gaussian peak around 50 keV originating from beta decays of ^{210}Pb in a good agreement with the measured background. This improved model estimates that the activities of ^{210}Pb and ^{3}H are the dominant sources of the backgrounds with an average level of 2.73±0.14 counts/day/keV/kg in the energy region of 1–6 keV, using COSINE-100 data with a total exposure of 97.7 kg·years.

1 Introduction

COSINE-100 is an NaI-based experiment for the direct detection of dark matter particles [1,2], with an array of 106 kg NaI(Tl) crystals. It has been operating at the Yangyang underground laboratory (Y2L) since September 2016 [3,4,5]. One of the COSINE-100 goals is to test DAMA/LIBRA's assertion of an observation of annual modulation signal with a statistical signifi-

[a]e-mail: ejjeon@ibs.re.kr
[b]e-mail: yjko@ibs.re.kr

cance that is now more than 12.9 σ in the energy region (2–6) keV [6,7,8]. There are several groups, such as DM-Ice [9,10], ANAIS [11,12], KamLAND-PICO [13], SABRE [14], and COSINUS [15], developing ultra-low-background NaI(Tl) crystals with the goal of reproducing the DAMA/LIBRA results. The DAMA/LIBRA collaboration claimed that the improved configuration lowers the energy threshold and reinforces the annual modulation signature at 9.5 σ C.L. in the energy region of 1–6 keV [8].

To verify the DAMA/LIBRA modulation signal, a complete understanding of the background energy spectrum is required. We have developed a background model by performing Monte Carlo simulations using the Geant4 toolkit (V.10.4.2) [16]. We used 1.7 years of COSINE-100 data taken from October 21, 2016 to July 18, 2018 with a 106 kg array of low background NaI(Tl) crystals. We used the measured spectrum obtained with a newly developed threshold of 1 keV electron equivalent energy [17]. To build a complete background model with the energy threshold as low as 1 keV, we precisely investigated the low-energy contribution from the surface ^{210}Pb contamination in the NaI(Tl) crystals [18], in addition to background simulations of internal radioactive contaminants, such as natural radioisotopes and cosmogenically activated isotopes inside NaI(Tl) and external background sources from the exterior of crystals. Moreover, an adjustment coefficient was applied to match the data and Monte Carlo (MC) simulations, taking the effect of the energy scale errors into consideration for the simulated spectrum at low energy.

2 The COSINE-100 experiment

The main detector of COSINE-100 is a 106 kg array of eight ultra-pure NaI(Tl) crystals (named as C1-C8) stacked in two layers. Each crystal is equipped with two 3–inch Hamamatsu R12669SEL photomultiplier tubes (PMTs). The NaI array is immersed in a 2200-liter liquid scintillator (LS) that serves both as an active veto and a passive shield. Four shielding layers exist comprising plastic scintillator panels, a lead-brick castle, a copper box, and a tank of liquid scintillator. The experimental setup is described in detail in Ref. [3]. All the used materials are properly assigned while constructing the geometry used for the simulations, as shown in Fig. 1.

We present here the background modeling to represent the initial 1.7 years of COSINE-100 data named as "SET2 data". Three crystals C1, C5, and C8 showed high background rates, twice as high as the other crystals. Also, C1 has a high noise rate and C5 and C8 have low light yields. All three crystals are excluded from this analysis. The total exposure used in this analysis is 97.7 kg·years with a total mass of 61.3 kg from the other five crystals.

To determine the light characteristics of the crystals and the liquid scintillator (LS), including light yields, energy scales, and energy resolutions, an energy calibration has been performed by tracking internal $\beta-$ and γ-ray peaks from radioactive contaminants in the crystals, as well as γ-ray sources. Internal background peaks at 49 keV from ^{210}Pb, 238 keV from ^{212}Pb, 295 keV and 352 keV from ^{214}Pb, 1462 keV from ^{40}K, 2614 keV from ^{208}Tl, 609, 1764, and 2204 keV from ^{214}Bi and the external background peak at 1173 keV from ^{60}Co are used for the high-energy calibration. A nonlinear detector response of NaI(Tl) crystals in the low energy region, as reported in Ref. [19], is studied and an empirical function is modeled to describe this nonlinearity. The charge-to-energy ratios of the calibration points for five NaI(Tl) crystals describe the nonlinear detector response that is fitted by an empirical function, as shown in Fig. 2; the peaks at 0.9 keV from ^{22}Na, 3.2 keV from ^{40}K, 25.5 keV from ^{109}Cd, 30.5 keV from ^{121}Te, 49 keV from ^{210}Pb, and 67.8 keV from ^{125}I are used for the low-energy calibration.

The event selection criteria for the 1 keV energy threshold [17] are applied in this analysis. Events classified as single-hit are for the ones that show more than 4 photoelectrons in only one of the crystals and none in any of the other crystals or the LS. Multiple-hit events are those with the LS signal and/or more than 4 photoelectrons in other crystals. The LS veto threshold was set at 20 keV for both single-hit and multiple-hit events.

The PMTs are configured to generate two readouts. Both signals from the high-gain anode and the low-gain 5th-stage dynode are stored as independent channels for all the events. The two readouts have different energy resolutions. The anode signals are used for low energy events with less than a boundary energy of 70 keV, while the 5th-stage dynode signals are used for those larger than the boundary.

3 Background simulations

The COSINE-100 simulation framework developed for the background spectra of the first 59.5-day data from the COSINE-100 detector ("SET1 data") [20] is used for the background simulations in this analysis. It is a Geant4-based simulation framework with a later version (10.4.2) than the Geant4 version 9.6.2 that was used in the previous analysis. The newer version better describes the non-Gaussian peak around 50 keV from the beta decay of ^{210}Pb to ^{210}Bi; only a small part, 4.3%, is due to the 46.5 keV gamma-ray line and most of the events in the peak are from the conversion electrons, Auger
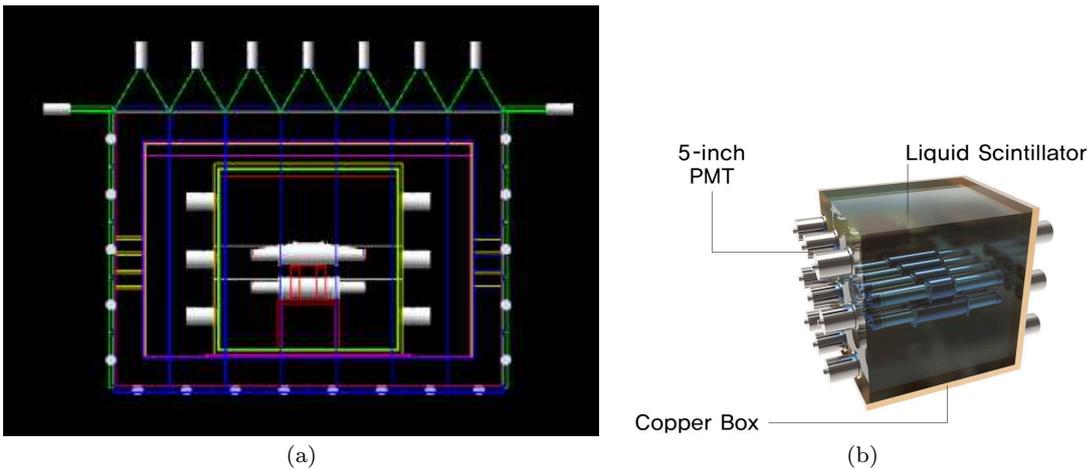
(a)   (b)

Fig. 1 Detector geometry (front view) used in the Geant4 simulation. (a) Two white-colored cylindrical shapes inside the center box represent the NaI(Tl) detectors supported by the acrylic frame (red) inside the liquid scintillator. (b) Eighteen 5-inch PMTs are attached to two sides of the copper box to detect LS-produced photons.
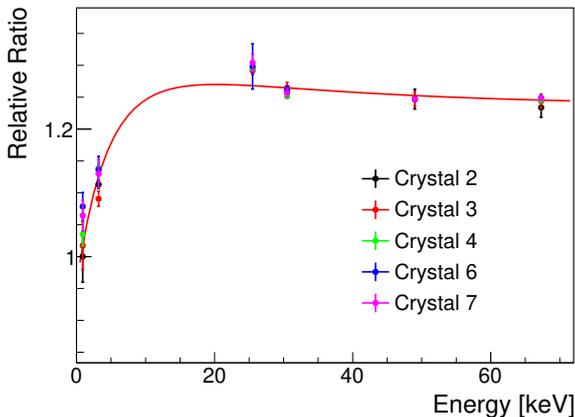

Fig. 2 Detector response to the calibration data points is described by an empirical function (red line) for five NaI(Tl) crystals at low energy.

electrons, and X-rays, followed by beta electrons from the decay to ^{210}Bi, which results in a non-Gaussian peak. It was not well reproduced by the simulations using the Geant4 version 9.6.2.

Each simulated event records all energies deposited in the crystals within an event window of 10 μs from the time when a decay is generated, to account for the conditions in the data acquisition system (DAQ) of the experimental setup [7]. Consecutive decays occurring in a short time, such as ^{212}Bi–^{212}Po decays with ^{212}Po's half-life of 300 ns may appear together in a 10 μs time window, resulting in pileup events. They are treated as a single event in the simulation. Based on this framework, we carried out Monte Carlo simulations for all the possible background sources to build a complete model of the background measurements with 1 keV energy threshold.

The simulated spectrum was convolved with an energy-dependent energy resolution function developed during the calibration.

3.1 Internal and external backgrounds

With the the first 59.5 days of SET1 data, the detector background was investigated with simulated background spectra from the internal radioactive sources, such as full decay chains of ^{238}U, ^{232}Th, ^{40}K, and ^{210}Pb inside the eight NaI(Tl) crystals assuming a chain equilibrium [3]. However, the background level may vary over the time if the internal activities are not in a chain equilibrium. We indeed found an evident increase in the ^{228}Th background level during the 1.7 years of SET2 data when compared with the SET1 result. To take broken chain effects of the background sources into account for the background simulation, the ^{238}U and ^{232}Th decay chains are treated as broken at the long-lived parts of the chain. The ^{238}U chain was broken into five distinct groups and the ^{232}Th chain was broken into three groups. The activities of the ^{238}U and ^{232}Th decay chains in the eight groups are treated as fitting parameters to quantify the unknown fractions of the background composition.

We simulated external background sources in the COSINE-100 experiment configuration: PMTs, greases, copper cases, bolts, cables, acrylic supports, liquid scintillator, copper box, and a steel structure that supports the lead block housing. Overall, the background spectrum is well matched to the data in the high-energy region, except for the peaks around 185 keV and 2.6 MeV in single-hit events. The background contribution due to the ^{235}U chain from the PMTs was treated in two groups as broken at the long-lived part of the chain and

the 185.7 keV γ–ray from the decay of ^{235}U in the first group was helpful to improve the modeling between 100 and 200 keV. This observation is similar to the one from other group [21] that reported the existence of ^{235}U in the same PMTs. The background peak around 2.6 MeV is well reproduced in multiple-hit events by the simulations while not in single-hit events for the same energy region, which indicates that there could be an unknown external component located a short distance away from the NaI(Tl) crystals. The inclusion of γ–rays from the decay of ^{208}Tl from the exterior of the crystals improved the background model around 2.6 MeV in the single-hit events; it is possible that there still exist background contributions from materials close to the detector.

3.2 Cosmogenic radioisotopes

Table 1 lists all the cosmogenic radioactive isotopes produced in the NaI(Tl) crystals in COSINE-100, as reported in Ref. [22], with their half-lives and decay modes; short-lived isotopes, for which half-lives are less than a year, are ^{125}I, ^{121}Te, ^{121m}Te, ^{123m}Te, ^{125m}Te, ^{127m}Te, and ^{113}Sn and long-lived isotopes are ^{109}Cd, ^{22}Na, ^{3}H, and ^{129}I. Since we use the 1.7-year data, the short-lived ($T_{1/2} < 1$ year) cosmogenic isotopes are not expected to contribute significantly to the crystals while the long-lived cosmogenic isotopes are expected to contribute more. There are three long-lived nuclides namely ^{3}H, ^{22}Na, and ^{109}Cd, which have low energy deposits and are, therefore, potentially troublesome. The beta-decay spectrum of tritium has an endpoint energy of 18 keV. The electron capture decay of ^{22}Na produces 0.87 keV emissions, and the electron capture decay of ^{109}Cd contributes peaks at 25.5 keV and around 3.5 keV

Table 1 Cosmogenic radionuclides in the NaI(Tl) crystals identified in other studies and considered here [22]. We list the contributing cosmogenic isotopes with their half lives and decay modes: β^+, β^-, electron capture (EC), and isomer transition (IT).

Cosmogenic isotopes	Half-life [23, 24, 25] (days)	Decay type & emissions energy
^{125}I	59.4	EC, 35.5+31.7=67.2 keV
^{121}Te	19.17	EC, 4.1–4.7 and 30.5 keV
^{121m}Te	164.2	EC, 4.1–4.7 and 30.5 keV
^{123m}Te	119.3	IT, 247 keV
^{125m}Te	57.4	IT, 145 keV
^{127m}Te	106.1	IT, 88 keV
^{113}Sn	115.1	EC, 3.7–4.2 and 28 keV
^{109}Cd	462	EC, 25.5 and 88 keV
^{22}Na	950	β^+, 511 and 1274.6 keV
^{3}H	4494	β^-
^{129}I	1.57×10^7 yr	β^-

which are at the binding energies of the Ag K-shell and L-shell electrons. It is thus essential to understand their background contributions to the low energy spectra regions, especially in the (1–6) keV dark matter signal region of interest (ROI). We, therefore, simulated backgrounds from cosmogenic radioactive isotopes, listed in Table 1. The simulated background spectra are used in the data fitting, by floating their unknown fractions and the fitted results are compared with the measurements reported in Ref. [22]. The details of these comparisons are discussed in Sect. 4.

As the presence of cosmogenic ^{129}I was introduced by DAMA/LIBRA with the estimated concentration of ^{129}I/^{nat}I = $(1.7 \pm 0.1) \times 10^{-13}$ [26], we included it in our background fitting model. Figure 3 shows the fitted simu-
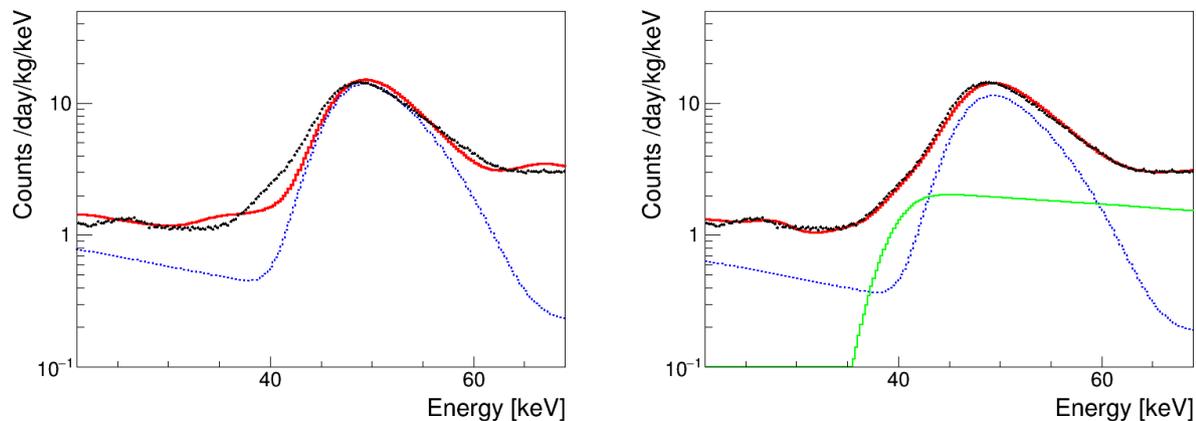

Fig. 3 Background modeling for low energy single hit events for Crystal 6. Background models not including ^{129}I (left) and including ^{129}I cosmogonic component (right) are shown. The solid green line corresponds to the ^{129}I isotope. The dashed blue line, the black dots, and the thick red line represent internal ^{210}Pb isotope, data, and the total MC, respectively.
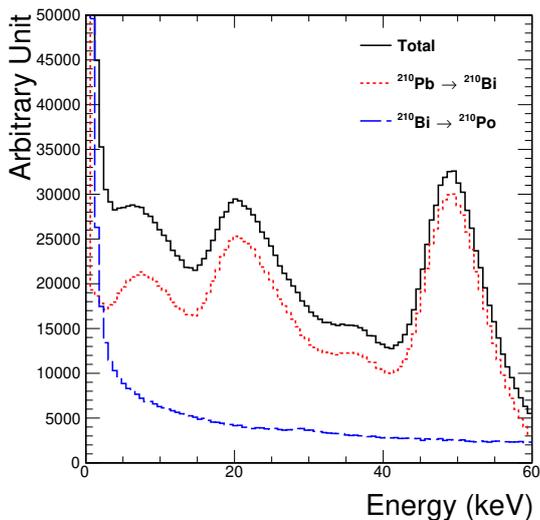
Fig. 4 Low-energy spectra due to the beta decays of ^{210}Pb that are distributed within the surface thickness of 1μm in the crystal. Further details are given in Sect. 3.3.

Fig. 5 Simulated energy spectra for the beta decays of ^{210}Pb within the surface of Crystal 7; we simulated the energy spectra for beta decays of ^{210}Pb that are exponentially distributed in the surface of Crystal 7 by following two exponential functions with mean depths of 1.39 μm (black solid line) and 0.107 μm (red dashed line).

lation spectra (a) not including of ^{129}I and (b) including of ^{129}I (green solid line). The simulated spectral shape of the ^{129}I in Crystal 6, as shown in Fig 3(b), improves the background modeling around 30 to 70 keV. This is because the beta decay of ^{129}I to ^{129}Xe* is followed by ^{129}Xe* transitioning to the stable ^{129}Xe isotope via the emission of a 39.6 keV γ–ray.

3.3 Surface ^{210}Pb

The Q value of the beta decay of ^{210}Pb to ^{210}Bi is 63.5 keV. The decay associates with low-energy emissions of electrons and γ/X–rays typically less than 60 keV. The light outputs of the low-energy events depend on the depth of ^{210}Pb distribution on the crystal surface. It has also been suggested that sources are attributed to the ^{222}Rn contamination that occurred anytime during the powder- and/or crystal-processing stages. To understand the energy spectra from the beta decays of ^{210}Pb, we simulated them by generating ^{210}Pb at random locations within the surface thickness of 1 μm in the crystal. The simulated spectra are depicted in Fig. 4, where each color represents the beta decays of ^{210}Pb (dotted red line) and ^{210}Bi (dashed blue line), respectively. The peaks at approximately 10 and 50 keV are attributed to the X-rays and 46.5 keV emissions together with about 4 keV mean energy of beta electrons from the decay to the ^{210}Bi metastable state. In addition, the conversion electrons contribute to the peaks at approximately 20 and 35 keV. These spectral features can be affected by the depth distribution of ^{210}Pb on
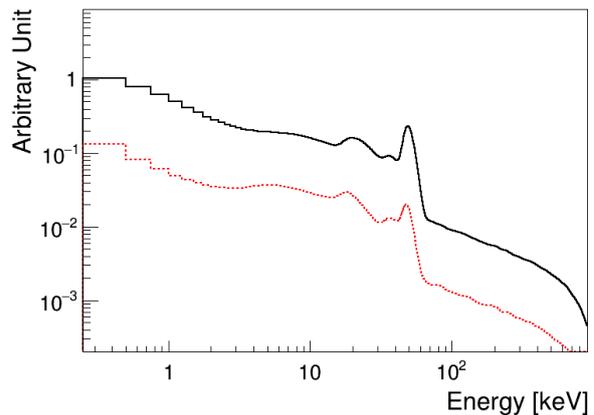
the crystal surface and, therefore, the depth profile of the surface ^{210}Pb contamination should be taken into account for the detector background in the low-energy region in particular for a low-background experiment using NaI(Tl) crystals.

We have studied the surface ^{210}Pb contamination with a test setup at Y2L using a NaI(Tl) crystal from the same ingot as C6 and C7. We measured its depth profile by using the measured spectra from both beta decay of ^{210}Pb and alpha decay of ^{210}Po at the decay sequence of the surface ^{210}Pb contamination that is obtained using a ^{222}Rn-contaminated crystal, as reported in Ref. [18]. Using this study, it was found that the low-energy spectrum of the surface ^{210}Pb contamination is primarily attributed to depth profiles of ^{210}Pb exponentially distributed within a shallow surface with a mean depth of (0.107±0.003) μm, as well as a deep surface with a mean depth of (1.39±0.02) μm. We thus simulated energy spectra from beta decays of ^{210}Pb that are exponentially distributed in the surface by following two exponential functions with the mean values of 1.39 μm and 0.107 μm for deep and shallow depths, respectively and the simulated spectra are used in the data fitting. The ratio of the amplitudes of the exponential distributions is treated as a floating parameter because it could be affected by the ^{222}Rn exposure. Figure 5 shows the simulated energy spectra of the surface ^{210}Pb contamination that is weighted by an exponential curve as a function of the surface depth. The black solid line represents the background spectrum of ^{210}Pb with the mean depth of 1.39 μm and the red dashed line represents the background spectrum of ^{210}Pb with the mean depth of 0.107 μm.
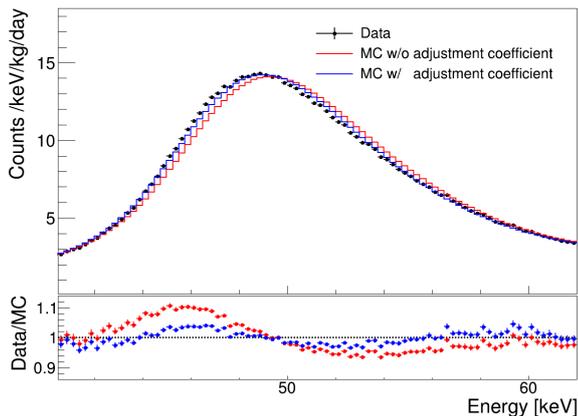
Fig. 6 Top panel shows Crystal 6 energy spectra of single-hit events in the low energy region. Black dots are data and the red (blue) line shows the total MC without (with) application of the adjustment coefficient in the background modeling fit. In the bottom panel, the red (blue) dots are the ratio of data to MC without (with) application of the adjustment coefficient.

3.4 Energy scale

We have improved the background modeling in the low energy region by precisely studying the low energy contributions from the background sources such as the surface ^{210}Pb contamination and long-lived cosmogenic isotopes. However, there is still a little mis-matching between data and MC spectra at low energies, which is because presumably the energy scales that are set separately for the anode readout and the dynode readout, based on linear fits of calibration data points, have errors propagated from the statistical uncertainty, as well as the nonlinear detector response, as described in Sect. 2. We, thus, consider an adjustment coefficient in the MC spectrum for the energy scale errors, using the method described in Sect. 3.4.1. Figure 6 shows the results considering the adjustment coefficient (blue line) and without considering the adjustment coefficient (red line) in the background modeling fit. It is shown that the background modeling has been improved with the adjustment coefficient.

3.4.1 Adjustment coefficient method

The energy scale set for the dynode readout is based on the linear fit of calibration data points and, thus, the energy E in the MC spectrum corresponding to the scaled energy of the dynode readout is adjusted as

$$E \rightarrow E(1 + \epsilon), \tag{1}$$

where ϵ is a coefficient that represents a change in energy. The ith bin content of the MC spectrum, B_i, can be

approximated as

$$B_i \rightarrow B_i + \epsilon \cdot \left. \frac{\partial B_i}{\partial \epsilon} \right|_{\epsilon=0}, \tag{2}$$

where we use a numerical approach to obtain the derivative as

$$\left. \frac{\partial B_i}{\partial \epsilon} \right|_{\epsilon=0} \approx \frac{B(E_i(1 + \delta\epsilon)) - B(E_i(1 - \delta\epsilon))}{2\delta\epsilon}, \tag{3}$$

where $\delta\epsilon$ represents a very small change in ϵ and E_i denotes the central value of the ith energy bin. A linear interpolation of the MC spectrum is used for the small variation of $\delta\epsilon$.

Since there is the nonlinear detector response modeled by the empirical function obtained in Sect. 2, at low energies, adjusting the energy in the MC spectrum corresponding to the scaled energy of the anode readout follows a different procedure from that of the dynode readout, and is expressed by

$$E \rightarrow E \left[1 + \epsilon \cdot \{ f(E) - C \} \right], \tag{4}$$

$$B_i \rightarrow B_i + \epsilon \cdot \{ f(E) - C \} \cdot \left. \frac{\partial B_i}{\partial \epsilon} \right|_{\epsilon=0}, \tag{5}$$

where $f(E)$ is the empirical function shown in Fig. 2 and C is a coefficient for a linear component.

4 Background modeling and results

In this analysis we used data collected between October 21, 2016 and July 18, 2018 ("SET2 data") with an energy threshold lowered to 1 keV. To model the measured energy spectrum ranged from 1 keV quantitatively, we have performed Geant4 Monte Carlo simulations for the background spectra, as described in Sect. 3, which are fitted to the measured data to quantify their background fractions.

We use a binned likelihood method with the following formula [27],

$$-2 \ln \lambda(\vec{\alpha}) = 2 \sum_{i=1}^{N_{\text{bins}}} \left[\sum_{j=1}^{N_{\text{components}}} \alpha_j S_{ij} - D_i \right. \tag{6}$$

$$+ D_i \ln \frac{D_i}{\sum_{j=1}^{N_{\text{components}}} \alpha_j S_{ij}} \right]$$

$$+ \sum_{j=1}^{N_{\text{components}}} \left(\frac{\alpha_j - m_j}{\sigma_j} \right)^2,$$

where $\lambda(\vec{\alpha})$ is the likelihood ratio in terms of the fractions of the MC components $\vec{\alpha} = (\alpha_1, \alpha_2, \cdots, \alpha_{N_{\text{components}}})$, D_i is the number of events in the ith energy bin of the data histogram and S_{ij} is the number of events in the ith bin of the jth simulation component. The last term
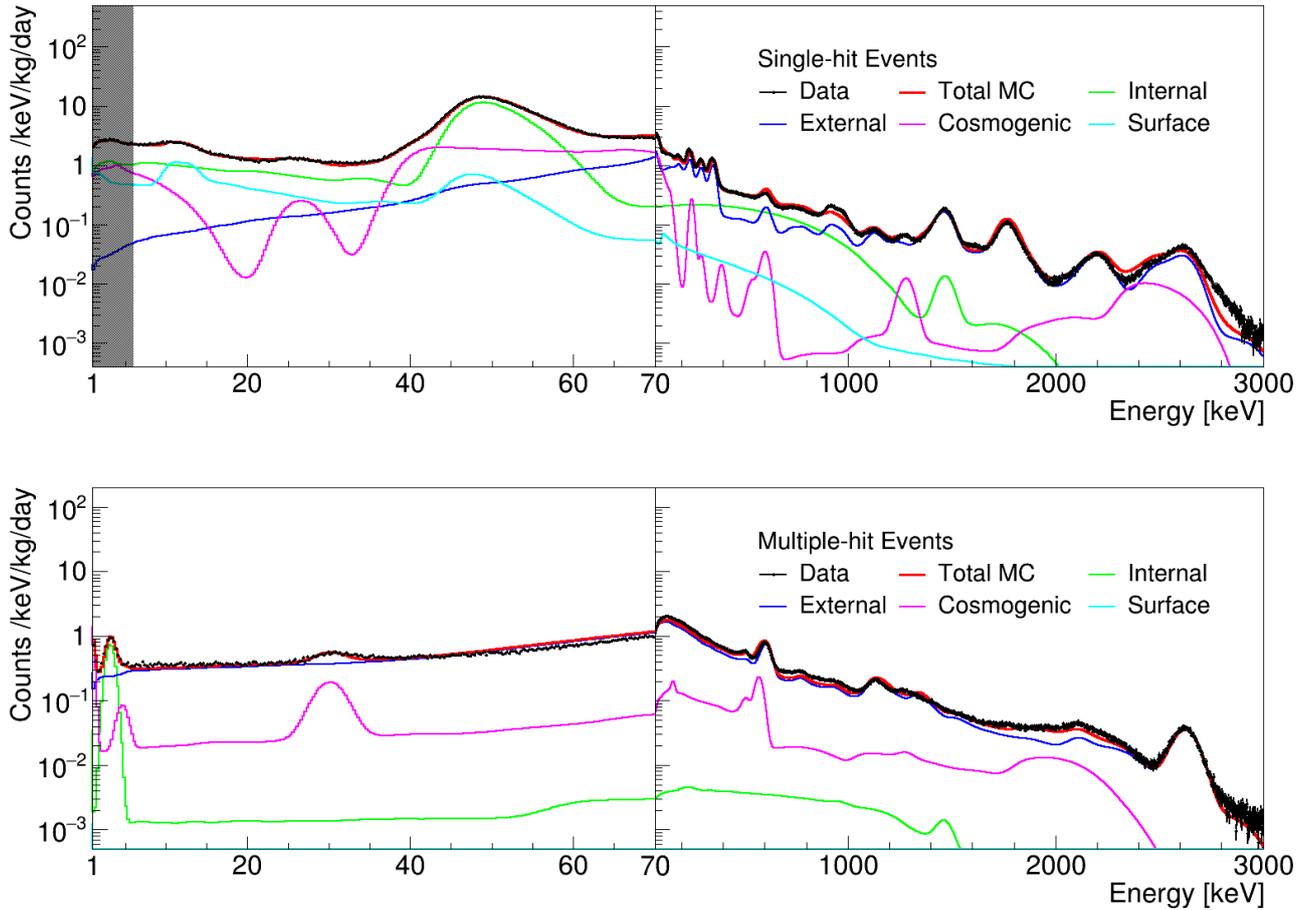
Fig. 7 The energy spectra of single-hit (top) and multiple-hit (bottom) events in Crystal 7. The MC was carried out to fit the measured data. The shaded area in the energy spectra of single-hit events is excluded from the data fitting.

denotes a prior for the fraction α_j of the jth component and is only active if there is a pre-measurement of this component; m_j and σ_j are the measured value and the error, respectively.

As mentioned in Sect. 3.4, low- and high-energy data are taken through anode and dynode channels, respectively, and they have different energy resolutions. Thus, we perform a four-channel simultaneous fit: single-hit low-energy, single-hit high-energy, multiple-hit low-energy, and multiple-hit high-energy spectra. In the four-channel fitting the energy ranges are set to be [6, 3000] and [1, 3000] keV for single-hit and multiple-hit events, respectively. The lower bound of the energy for multiple-hit events is extended to 1 keV based on the study of lowering the energy threshold, reported in Ref. [17]. The lower bound for the single-hit events is set to 6 keV as not to bias the WIMP signal in the ROI.

Figure 7 shows the measured and simulated background spectra of Crystal 7 in both low and high energy regions. The spectra for single-hits and multiple-hits are shown in the top and the bottom, respectively. One can see that the SET2 data is well reproduced overall except for the energy region higher than ∼2.7 MeV for single-hit events. This issue is presumed to be due to the absence of one or more components that could better account for the energy range above 2.7 MeV, and the analysis will continue to figure out the issue. The agreement between the measured and fitted background spectra for both single- and multiple-hit events of Crystal-2, 3, 4, and 6 in both low and high energy regions is as good as shown for Crystal 7.

In the modeling fit, to distinguish between surface and bulk ^{210}Pb components, we used depth profiles of ^{210}Pb distributed within a shallow surface with the mean depth of 0.107 μm, as well as a deep surface with the mean depth of 1.39 μm; their fractions are allowed to float. As a result of the fit, the surface ^{210}Pb contamination of three Crystals (2, 3, and 4) is primarily
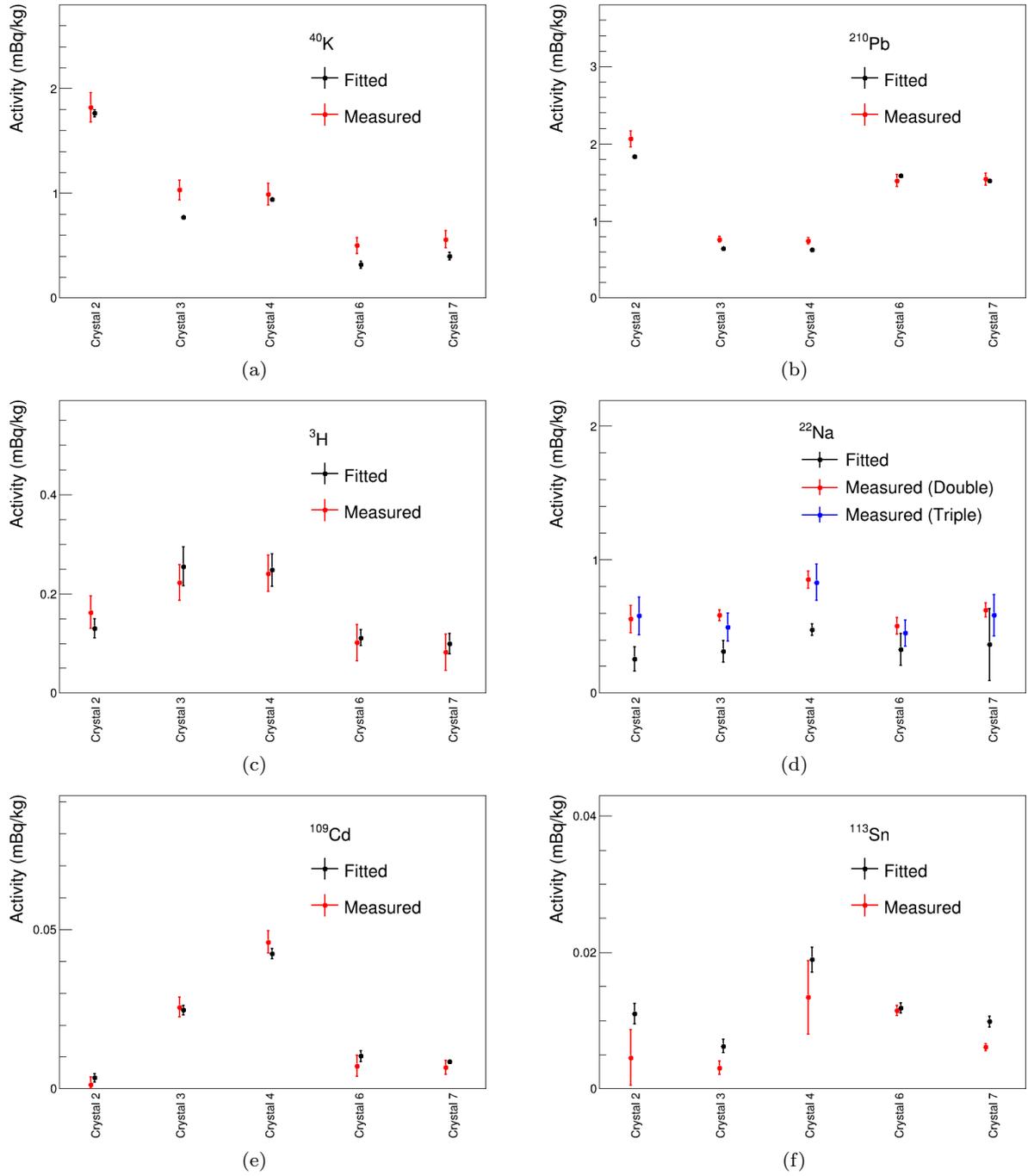
Fig. 8 Comparison of the measured [3][20][22] and the fitted activity levels in five NaI(Tl) crystals.

attributed to the deep depth profile and for Crystal 7 is primarily attributed to the shallow depth profile. The depth distribution of ^{210}Pb for Crystal 6 consists of both shallow and deep depth profiles. As studied in Ref. [18], surface ^{210}Pb contamination could be affected by ^{222}Rn exposure.e

In Fig. 8(a) and (b), we compared the fitted activities of internal ^{40}K and ^{210}Pb to their measured levels

for the five crystals with an agreement at the ∼20% level. Since we used the 1.7-year data, the short-lived ($T_{1/2} < 1$ year) cosmogenic isotopes are not expected to contribute significantly to the crystals, while the long-lived cosmogenic isotopes such as ^{3}H, ^{22}Na, and ^{109}Cd are expected to contribute more. The fitted activities of long-lived cosmogenic isotopes: ^{3}H, ^{22}Na, and ^{109}Cd for the five crystals are compared with the measured ones,

Table 2 Background contributions in the energy range of 1 to 6 keV. There are only statistical uncertainties for the data row, and uncertainties for other rows are from the modeling.

| [Unit: Counts/keV/kg/day]		Crystal 2	Crystal 3	Crystal 4	Crystal 6	Crystal 7
Data		2.783 ± 0.010	2.945 ± 0.010	2.882 ± 0.007	2.350 ± 0.008	2.492 ± 0.009
Total simulation		2.819 ± 0.189	2.989 ± 0.369	2.930 ± 0.325	2.367 ± 0.324	2.504 ± 0.210
Internal	^{210}Pb	1.224 ± 0.006	0.417 ± 0.010	0.400 ± 0.012	1.026 ± 0.017	0.999 ± 0.008
	^{40}K	0.199 ± 0.004	0.081 ± 0.002	0.104 ± 0.001	0.037 ± 0.004	0.046 ± 0.004
	Others	0.0103 ± 0.0001	0.0102 ± 0.0001	0.0042 ± 0.0002	0.0074 ± 0.0001	0.0048 ± 0.0001
Surface ^{210}Pb	Crystal	0.178 ± 0.101	0.205 ± 0.194	0.230 ± 0.198	0.268 ± 0.297	0.513 ± 0.131
	Teflon	0.028 ± 0.005	0.081 ± 0.008	0.034 ± 0.007	0.044 ± 0.004	0.051 ± 0.004
Cosmogenic	^{3}H	1.071 ± 0.160	2.052 ± 0.313	1.964 ± 0.258	0.888 ± 0.128	0.798 ± 0.164
	^{113}Sn	0.023 ± 0.003	0.013 ± 0.002	0.039 ± 0.004	0.024 ± 0.002	0.020 ± 0.002
	^{109}Cd	0.009 ± 0.003	0.064 ± 0.004	0.110 ± 0.004	0.027 ± 0.004	0.022 ± 0.002
	Others	0.022 ± 0.003	0.030 ± 0.001	0.019 ± 0.001	0.013 ± 0.002	0.015 ± 0.004
External ($\times 10^{-2}$)		5.290 ± 0.103	3.563 ± 0.039	2.697 ± 0.037	3.358 ± 0.089	3.374 ± 0.062
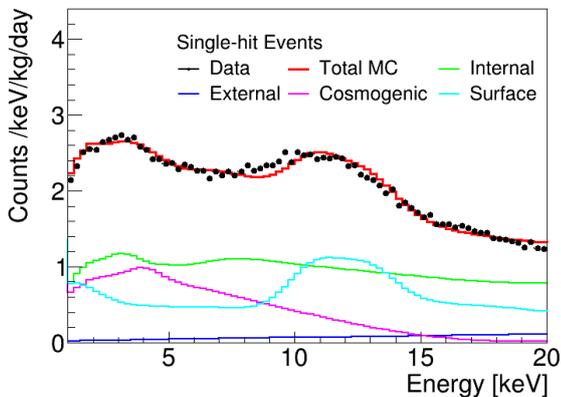
Fig. 9 The low-energy spectra of single-hit events in Crystal 7. The measured energy spectrum is compared with the total of the simulations. The range of 1 to 6 keV in the MC spectrum is extrapolated from the modeling.

reported in Ref [22], as shown in Fig. 8(c),(d),(e); these values are in reasonable agreement with the measurements that averaged measured activities in the 1.7 years of data. ^{109}Cd contributes peaks at 25.5 and ~3.5 keV by electron capture decay and, similarly, there is an isotope of ^{113}Sn that produces 28 keV and 3.7~4.2 keV emissions by the electron capture decay, as described in Table 1. We took into account the effect of ^{113}Sn in the modeling fit. However, because ^{113}Sn has a short half-life of 115.1 days, the 1.7 year period is long enough to reduce its activity to a negligible level while ^{109}Cd has 562 days of half-life and enough activity levels when produced. As a result of the fit, they are compared with the measurements in Fig. 8(f).

Based on the background model, we found the background levels for the five NaI(Tl) detectors in unit of dru (counts/day/keV/kg) in 1–6 keV as listed in Table 2. The dominant background contributions are from ^{210}Pb and ^{3}H. Figure 9 shows the low-energy spectra of single-hit events of Crystal 7 in the 1–20 keV energy region. The range of 1 to 6 keV in the MC spectrum is extrapolated from the modeling. The measured and simulated results are in a good agreement.

5 Conclusion

COSINE-100 has been taking data at Y2L from October 21, 2016. We present the background model for the WIMP search during the first 1.7 years of COSINE-100 data. Our previous analysis with 59.5-day data showed that ^{210}Pb and ^{3}H produce the dominant contributions in the energy region of 2–6 keV. As we lowered the threshold to 1 keV, the background modeling was carried out accordingly. The model includes background contributions from both internal and external sources, including cosmogenic radionuclides and surface ^{210}Pb contamination. To improve the background model with the energy threshold as low as 1 keV, we used a depth profile of the surface ^{210}Pb contamination that is provided by the measurement with a test setup at Y2L. We also considered the effect of the energy scale errors propagated from the statistical uncertainty and the nonlinear detector response for the simulated spectrum at low energy. With this improved background model, the overall energy spectrum summed over all the simulation results is well matched to the measured data not only for single-hit events but also for multiple-hit events. The improved model estimates the averaged background level of 2.73 ± 0.14 counts/day/keV/kg in the energy region of 1–6 keV dominated by ^{210}Pb and ^{3}H for the five crystals of COSINE-100 during the 1.7 years period of SET2 data with a total exposure of 97.7 kg·years.

Acknowledgments

References

1. R. Gaitskell, Annu. Rev. Nucl. Part. Sci. 54, 315(2004).
2. L. Baudis, Phys. DarkUniv. 1, 94 (2012).
3. G. Adhikari *et al.*, Eur. Phys. J. C **78** (2018) 107.
4. G. Adhikari *et al.*, Nature **564** (7734) (2018) 83-86.
5. G. Adhikari *et al.*, Phys. Rev. Lett. **123**, 031302 (2019).
6. R. Bernabei *et al.*, Int. J. Mod. Phys. D **13** (2004) 2127.
7. R. Bernabei *et al.*, Eur. Phys. J. C **73** (2013) 2648.
8. R. Bernabei *et al.* (DAMA/LIBRA), Nucl. Phys. At. Energy **19** (2018) 307. arXiv:1805.10486.
9. J. Cherwinka *et al.*, (DM-Ice Collaboration), Phys. Rev. D **90** (2014) 092005.
10. E. Barbosa de Souza *et al.* (DM-Ice Collaboration), Phys. Rev. D **95** (2017) 032006.
11. J. Amare *et al.*, Nucl. Instrum. Meth. Phys. Res., Sect. A **742** (2014) 187.
12. J. Amare *et al.*, Phys. Rev. Lett. **123** (2019) 031301.
13. K. Fushimi *et al.*, Physics Procedia **61** (2015) 67.
14. C. Tomei *et al.* (SABRE Collaboration), Nucl. Instrum. Meth. A **845** (2017) 418.
15. G. Angloher *et al.*, Eur. Phys. J. C **76** (2016) 441.
16. S. Agostinelli *et al.*, Nucl. Instrum. Meth. Phys. Res., Sect. A **506** (2003) 250.
17. G. Adhikari *et al.* (COSINE-100 Collaboration), arXiv:2005.13784.
18. G.H, Yu.*et al.*, Astropart. Phys. **126** (2021) 102518.
19. L. Swiderski et al., Nucl. Instruments Methods Phys. Res. Sect. A Accel. Spectrometers, Detect. Assoc. Equip. **705** 42–46, 2013.
20. P. Adhikari *et al.*, Eur. Phys. J. C **78** (2018) 490.
21. J. Amare *et al.*, Eur. Phys. J. C **76** (2016) 429.
22. E. Barbosa de Souza *et al.* (COSINE-100 Collaboration), Astropart. Phys. **115** (2020) 102390.
23. Decay Data Evaluation Project, `http://www.nucleide.org/DDEP_WG/DDEPdata.htm`
24. S. Ohya, Nucl. Data Sheets 111, 1619 (2010).
25. WWW Table of Radioactive Isotopes, `http://nucleardata.nuclear.lu.se/toi/`
26. R. Bernabei *at al.*, The DAMA/LIBRA apparatus, Nucl. Instrum. Meth. A **592** (2008) 297.
27. P.A. Zyla *et al.* (Particle Data Group), Prog. Theor. Exp. Phys. **2020** (2020) 083C01.